Adjustable quantum interference oscillations in Sb-doped Bi_2Se_3 topological insulator nanoribbons

Hong-Seok Kim[1, ‖], Tae-Ha Hwang[1, ‖], Nam-Hee Kim[1], Yasen Hou[2], Dong Yu[2], H.-S. Sim[3], Yong-Joo Doh[1*]

[1]Department of Physics and Photon Science, School of Physics and Chemistry, Gwangju Institute of Science and Technology (GIST), Gwangju 61005, Korea

[2]Department of Physics, University of California, Davis, CA 95616, USA

[3]Department of Physics, Korea Advanced Institute of Science and Technology, Daejeon 34141, Korea

Corresponding Authors

[*]E-mail: yjdoh@gist.ac.kr

Author contributions

‖ These authors contributed equally to this work.

KEYWORDS: Topological insulator nanoribbon, Sb-doped Bi_2Se_3 nanoribbons, topological surface state, Aharonov–Bohm oscillations, Altshuler–Aronov–Spivak oscillations, channel length effect

Abstract

Topological insulator (TI) nanoribbons (NRs) provide a unique platform for investigating quantum interference oscillations combined with topological surface states. One-dimensional subbands formed along the perimeter of a TI NR can be modulated by an axial magnetic field, exhibiting Aharonov–Bohm (AB) and Altshuler–Aronov–Spivak (AAS) oscillations of magnetoconductance. Using Sb-doped Bi_2Se_3 TI NRs, we discovered that the relative amplitudes of two quantum oscillations can be tuned by varying the channel length. The gate-voltage-dependent phase alternation of AB oscillations is discernible even for a 70-μm-long channel. Analyses based on ensemble-averaged fast Fourier transform of magnetoconductance curves revealed exponential temperature dependences of AB and AAS oscillations, which are due to thermal broadening and thermal dephasing effects, respectively. Our observations indicate that the channel length in a TI NR can be a useful control knob for tailored quantum interference oscillations, which would be promising for developing various topological quantum devices.

The quantum interference effects of a charged particle's wave function provide the cornerstone for mesoscopic physics, as they affect the development of quantum information devices. The Aharonov–Bohm (AB) effect[1] resulting from the coupling of an electromagnetic potential with the phase of a charged particle's wave function can be utilized to investigate the phase shift between two coherent electron beams propagating around a magnetic field. The solid-state AB effect, known as AB oscillations (ABOs), has been demonstrated in various quasi-ballistic ring structures fabricated using normal metals[2], quantum wells[3], and graphene[4]. The conductance is modulated periodically as a function of magnetic flux, Φ through a loop with a period of the flux quantum, i.e., $\Phi_0 = h/e$, where h is the Planck constant, and e is the elementary charge. For a weakly disordered ring[5] or a hollow metallic cylinder[6, 7] including carbon nanotubes[8] and core/shell nanowires[9], the $h/2e$–periodic oscillations, which are known as Altshuler–Aronov–Spivak (AAS) oscillations[10], dominate h/e oscillations. The AAS oscillations are caused by the interference between a pair of time-reversed paths propagating clockwise and counterclockwise around the magnetic flux[7].

Topological insulator (TI) nanoribbons (NRs) provide a novel platform for investigating mesoscopic quantum interference effects combined with a nontrivial topological order[11, 12]. Because three-dimensional (3D) TIs are bulk insulators with gapless spin-textured surface states[13], TI NRs can be regarded as hollow metallic cylinders, whose surface states are topologically protected from time-reversal invariant perturbations[13]. Considering quantum confinement along the perimeter of TI NRs, the surface states form discrete one-dimensional (1D) subbands exhibiting flux-dependent dispersion[14], which comprises the AB phase of $2\pi\Phi/\Phi_0$ owing to the axial magnetic field (B_{axial}) and the Berry phase of π caused by the spin–momentum locking effect in TIs[11, 12]. When the axial flux through the core of a TI NR becomes an odd multiple of the half-flux quantum, the AB phase shift cancels the Berry phase and hence restores a topologically protected zero-gap 1D mode[13, 14], which can host the Majorana bound states[15]. Resultantly the density of states of the surface states is modulated by B_{axial} with a period of Φ_0, resulting in magnetoconductance (MC) oscillations in TI NRs, whereas the MC maxima occur at the integer (0-ABO) or half-integer (π-ABO) multiples of Φ_0, depending on the location of the Fermi level[13, 14].

Thus far, topological ABOs have been observed in various NRs made of Bi_2Se_3[14, 16, 17], Sb-doped Bi_2Se_3[18], Bi_2Te_3[19, 20, 21], and 3D Dirac semimetals[22, 23]. However, several unresolved issues remain. First, AAS-type MC oscillations are concomitantly observed with ABOs in many cases[14, 16, 19, 23]; however, their absence has also been reported[18, 21, 22] without a clear explanation. Furthermore, for the observations of $h/2e$-periodic MC oscillations, two conflicting explanations have been suggested: the weak antilocalization (WAL) effect along the perimeter of the TI NR in the diffusive regime[14, 16, 19] or the second harmonic of ABOs occurring in the quasi-ballistic regime[17, 20]. In addition, the temperature dependence of ABOs follows the diffusive[16, 19] or quasi-ballistic[14, 17, 20] transport behavior for the same kind of NRs with similar geometric dimensions. Finally, the crossover between AB and AAS oscillations in TI NRs is expected based on theory[11, 24]; however, its experimental verification has not been performed yet.

Herein, we present an extensive experimental study of AB and AAS oscillations obtained from Sb-doped Bi_2Se_3 TI NRs with various channel lengths (L_{ch}) on the same NR. Their axial MC oscillations were measured as a function of gate voltage (V_g) and temperature (T), whereas their oscillation amplitudes were analyzed using the ensemble-averaged fast Fourier transform (FFT) method to avoid sample-specific features. We observed the crossover behavior between AB and AAS oscillations and discovered that their respective oscillation amplitudes were adjustable depending on the channel length of the TI NR. AAS oscillations were absent for channel lengths shorter than the perimeter length (L_p), and their length dependence was consistent with theoretical expectations based on WAL corrections[11] along the perimeter of TI NR. ABOs were discernible even for the 70 μm-long channel; furthermore, the V_g-dependent alternations of 0- and π-ABOs, a characteristic feature of topological ABOs[20], were evident in all segments with L_{ch} = 1–70 μm. Our observations suggest that the L_{ch} of the TI NR can be a control knob to alter the quantum electronic transport from quasi-ballistic to diffusive regimes, which would be advantageous for investigating quantum interference effects associated with topological surface states.

Results

Channel length dependence of AB and AAS oscillations. Figure 1a shows the scanning electron microscopy (SEM) image of the Sb-doped Bi_2Se_3 TI NR device (**D2**) with various channel lengths fabricated on the same NR. The geometric dimensions of the TI NR are provided in Supplementary Table 1. When an external magnetic field is applied along the NR axis, the axial MC, $G(B_{axial})$ curve shows oscillatory behavior superposed on a parabolic background (see Supplementary Fig. 4). After subtracting the smooth background signal from the MC data, we obtained the periodic oscillations of MC variation, δG, as shown in Fig. 1c. The oscillation period is obtained to be ΔB_{axial} = 0.075 T, which corresponds to $\Phi = 1.05\Phi_0$ considering a 5 nm-thick native oxide layer[19, 23] formed on the surface of the TI NR (see Supplementary Fig. 2). In addition, two $\delta G(B_{axial})$ curves obtained at V_g = -2.5 and -2.8 V show 0- and π-ABOs, respectively. Figure 1d shows the color plots of $\delta G(B_{axial})$ curves as a function of V_g for different L_{ch} values on the same TI NR. For L_{ch} = 1 μm, the ABO phase alternates between 0 and π with varying V_g, exhibiting a checkerboard-like pattern with sharp boundaries. Similar rectangular patterns were obtained from different devices (**D1**) with L_{ch} = 1 μm over a wide range of V_g (see Supplementary Fig. 5), revealing the out-of-phase relationship between two $\delta G(V_g)$ curves for $\Phi = 0$ and $0.5\Phi_0$ as supporting evidence for topological ABOs[11, 20] in the TI NRs. The FFT analysis for a 1-μm-long segment in **D2**, as shown in Fig. 1e, shows a single peak corresponding to the h/e-periodic oscillations of δG, indicating that the axial MC curves obtained from the short-channel devices were dominated by the ABOs only. Because the $\delta G(B_{axial})$ curve was extremely sensitive to V_g, the FFT spectrum in Fig. 1e represents the ensemble average of the total 51 FFT spectra obtained at different V_g with a constant increment of $\Delta V_g = 100$ mV.

When the channel length was increased on the same TI NR, the overall amplitude of the $\delta G(B_{axial})$ curve decreased, and the shape of the checkerboard pattern deformed from rectangular to elliptical (see Fig. 1d). In particular, the positive δG patterns elongated along the V_g axis, whereas their widths reduced along the B_{axial} axis. Such deformations in the $\delta G(B_{axial}, V_g)$ plots are attributed to the occurrence of $h/2e$-periodic MC oscillations in the long-channel devices, which are superposed on the topological ABO patterns in the TI NR. Contrary to the ABOs showing V_g-dependent phase alternation, the $h/2e$-periodic MC oscillations showed their conductance maxima at integer multiples of $\Phi_0/2$, irrespective of V_g. The V_g-independent behavior of the $h/2e$-periodic oscillations suggests that they were caused by the AAS effect rather than the second-harmonic AB effect.

The ensemble-averaged FFT results with different L_{ch} values are shown in Fig. 1e, in which two peaks corresponding to the h/e- and $h/2e$-periodic oscillations are shown. The peak heights of the FFT spectra are shown in Fig. 1f as a function of L_{ch}. The FFT peak height corresponding to the ABOs decreases monotonically with increasing L_{ch}, whereas the AAS oscillations exhibits a nonmonotonous channel-length dependence: nearly absent for L_{ch} = 1 μm, maximized at L_{ch} = 2−3 μm, and decreases gradually for $L_{ch} > 3$ μm. The absence of AAS oscillations in the short-channel device is attributed to an incomplete formation of the time-reversed path[11] along the perimeter of the TI NR for $L_{ch} < L_p$, where L_p is 1.2 μm for **D2**. The solid line, which agrees well with the experimental data, is the best fit of the WAL correction[11] along the perimeter of the TI NR (see Methods), indicating that our observed $h/2e$-periodic oscillations for $L_{ch} > L_p$ were caused by AAS oscillations in the TI NR in the weak-disorder limit.

The decreasing amplitudes of the ABOs with increasing L_{ch} can be explained by the effect of ensemble averaging of the uncorrelated ABOs in the TI NRs. Because the TI NRs are topologically analogous to hollow metallic cylinders[20], the long-channel device can be considered as a series array of metallic AB loops[5] exhibiting random polarity of $\delta G(B_{axial} = 0)$ at fixed V_g. Here, the number of loops, N_{AB}, is expressed as $N_{AB} = L_{ch}/L_\phi$, where L_ϕ is the phase coherence length[25]. We obtained L_ϕ = 465 nm at T = 3 K from the WAL analysis of perpendicular MC in the TI NRs (see Supplementary Fig. 6). It is well known that the stochastic average of ABOs in a chain of N_{AB} loops results in the suppression of the oscillation amplitude, which is proportional to $N_{AB}^{-3/2}$, considering the connecting leads between the loops[5, 25]. Hence, we fitted a $L_{ch}^{-3/2}$ function to the ensemble-averaged FFT peak heights of the h/e-periodic oscillations (see the dashed line in Fig. 1f), and it agrees reasonably well with the experimental data except L_{ch} = 1 μm.

More interestingly, AB and AAS oscillations were also observed in an extremely long NR segment of L_{ch} = 70 μm, as shown in Fig. 2a. To the best of our knowledge, this is the longest NR exhibiting ABOs thus far. The $\delta G(B_{axial})$ curve in Fig. 2c shows the coexistence of AB and AAS oscillations, exhibiting the V_g-dependent alternation of 0- and π-ABOs as well. The color plot of $\delta G(B_{axial}, V_g)$ shows the checkerboard pattern of the ABO overlaid with AAS oscillations. The $h/2e$-periodic oscillations became insignificant at B_{axial} fields greater than ~ 0.5 T, which is due to the suppression of coherent backscattering induced by time-reversal symmetry breaking[9, 14]. By contrast, the ABO persisted up to greater B_{axial} fields, as depicted in Fig. 2c, because the AB phase was due to the coherent forward scattering of the surface electrons on the TI NRs. It is noteworthy that the TI NR segment with L_{ch} = 70 μm corresponds to a chain of AB loops with N_{AB} ~ 151, indicating that the visibility of the ABO in the TI NR is robust to the ensemble average compared with the metallic loops[5]. The robustness of the TI NR is attributable to the extremely thin topological-surface-state thickness (i.e., < 6 nm, as estimated from the full-width at half maximum of the FFT spectral peak[16]) and the uniform cross-sectional area of the TI NR used in this study (see Supplementary Fig. 3). Moreover, the modulation of the density of states in the 1D subbands of the TI NR, which is due to the zero-gap 1D mode occurring at half-integer multiples of Φ_0, is also resonsible for the robust ABOs. For the segment with L_{ch} = 5 μm, similar features were observed, as shown in Fig. 2b, except the relative ratio between the AB and AAS oscillation amplitudes.

The ensemble-averaged FFT spectra with different L_{ch} values, normalized by the sum of the two peak heights of h/e- and $h/2e$-periodic oscillations, are shown in Fig. 2d. As mentioned previously, the ABOs dominated over the 1-μm-long channel device with N_{AB} ~ 2, which is characteristic of quasi-ballistic transport in TI NRs. By contrast, the quantum interference oscillations in the 70-μm-long channel with N_{AB} ~ 151 were dominated by AAS oscillations with WAL corrections, indicating that the long-channel TI NRs exhibited diffusive quantum transport at low temperatures. For the 5-μm-long channel (N_{AB} ~ 11), the FFT peak height of the AB oscillations was similar to that of the AAS oscillations, indicating a crossover from ballistic to diffusive quantum transport in the TI NRs. Although temperature- or disorder-driven crossover between AB and AAS oscillations has been predicted theoretically[26, 27], it has not been demonstrated experimentally yet. Our observations indicate that those quantum interference oscillations can be tuned by adjusting the channel length of the TI NR, which is in the weak-disorder limit. Meanwhile, the ensemble-averaged FFT spectrum can be used to identify the electrical transport regime of the TI NRs at an arbitrary disorder strength. We expect the channel-length-dependent topological quantum interferometers of the TI NR to be useful for investigating various features of topological quantum devices combined with superconductivity[28, 29], ferromagnetism[30, 31], or nanomechanics[32].

Temperature dependence of AB and AAS oscillations The color plots of $\delta G(B_{\mathrm{axial}}, V_{\mathrm{g}})$ with different L_{ch} values as a function of temperature are shown in Figs. 3a–c. The overall amplitude of $\delta G(B_{\mathrm{axial}}, V_{\mathrm{g}})$ diminished owing to thermal fluctuations. Furthermore, the boundaries of the checkerboard patterns became highly irregular at higher temperatures for L_{ch} = 2 μm in **D2**, as shown in Fig. 3a. However, the other segments in **D6**, maintained their pattern shapes at high temperatures (see Figs. 3b–c), which will be discussed later. The ensemble-averaged FFT spectra obtained at different temperatures are shown in Figs. 3d–f, showing two peaks corresponding to the h/e- and $h/2e$-periodic oscillations. The FFT amplitudes for the $\delta G(B_{\mathrm{axial}})$ curves with different V_{g} were averaged over 21 (27) traces with the increment of ΔV_{g} = 100 (50) mV for the 2-μm-long segment in **D2** (5- and 70-μm-long segments in **D6**).

Figures 3g–i show the heights of the two FFT peaks as a function of temperature. Linear T dependences of the FFT peak heights in the semi-log plot indicate that the amplitudes of the AB and AAS oscillations in the TI NRs, regardless of L_{ch}, decay exponentially with temperature, resulting in $\delta G_i(T) \sim \exp(-b_i T)$, where b_i is the damping parameter (i signifies h/e or $h/2e$ oscillations) of each quantum oscillation. Previous studies using the single-trace FFT method reported exponential temperature dependence[14, 17, 20, 21] or a $T^{-1/2}$ behavior[16, 19] for the amplitude of the ABOs in TI NRs. In this study, we observed the exponential T dependence of both AB and AAS oscillations using the ensemble-averaged FFT method to avoid any confusion caused by universal conductance fluctuations[33] or V_g-dependent voltage fluctuations due to residual charges on the substrate[34].

The exponential temperature dependence of the ABO amplitude, which was also observed in a ballistic AB ring[34, 35] comprising two-dimensional electron gas, is attributed to the averaging effect of temperature-induced phase shifts near the Fermi energy[36]. The thermal broadening effect can be described by $\exp(-b_{h/e}T) = \exp(-k_B T/E_c)$, where k_B is the Boltzmann constant, $E_c = \hbar v_F/L_p$ the correlation energy, $\hbar$ the reduced Planck's constant, and v_F the Fermi velocity[14, 35]. For L_{ch} = 2 μm in **D2**, we obtained E_c = 165 μeV using L_p = 1.2 μm and $v_F = 3 \times 10^5$ m/s (see Supplementary Note 3). Subsequently, the AB damping parameter was calculated to be $b_{h/e,cal} = k_B/E_c$ = 0.52 K^{-1}, which is similar to the experimental value of $b_{h/e}$ = 0.56 K^{-1} in Fig. 3g. For other NR segments in **D6**, we obtained E_c = 251 μeV and $b_{h/e,cal}$ = 0.34 K^{-1} using L_p = 0.79 μm, which agreed well with the experimental values of $b_{h/e}$ = 0.35 and 0.34 K^{-1} for L_{ch} = 5 and 70 μm, respectively, as shown in Figs. 3h–i. The smaller L_p for the segments in **D6** resulted in a larger E_c than that obtained from **D2**; hence, the ABO in **D6** was more robust against thermal fluctuations and preserved the pattern shapes at high temperatures, as shown in Figs. 3b–c.

Although the amplitude of the AAS oscillations exhibited an exponential behavior of $\exp(-b_{h/2e}T)$, similar to those shown in Figs. 3g–i, its underlying mechanism differed from that of the ABO. Because the AAS oscillations are due to the quantum interference between two time-reversed paths, the phase shift for the same path is zero; therefore, the AAS oscillations are insensitive to the thermal broadening effect[35]. By contrast, thermal dephasing through inelastic electron–electron scattering results in a shorter phase coherence length[35]; therefore, the expression $\exp(-b_{h/2e}T) = \exp(-2L_p/L_{\varphi,c}(T))$ holds, where $L_{\varphi,c}$, which is the phase coherence length along the circumference of the TI NR, was used instead of L_φ estimated from the perpendicular MC data. Using the relation $L_{\varphi,c} = 2L_p/b_{h/2e}T$, the circumferential coherence length at $T = 1$ K is estimated to be $L_{\varphi,c}(T = 1\text{ K}) = 2.8$, 4.2, and 3.4 μm for $L_{ch} = 2$, 5, and 70 μm, respectively, from the experimental values of $b_{h/2e}$ in Figs. 3g–i. It is noteworthy that our observed $L_{\varphi,c}(T = 1\text{ K})$ is two to five times longer than L_p, which is sufficient to assure phase-coherent quantum transport along the circumference of the TI NRs. Moreover, our $L_{\varphi,c}$ values are two to three times larger than those reported previously[17, 20], indicating that the TI NRs in this study are in the weak-disorder limit. Furthermore, $L_{\varphi,c}(T = 1\text{ K})$ is much longer than $L_\varphi(T = 1\text{ K}) = 830$ nm obtained from the perpendicular MC data, inferring that the L_φ of the TI NR can be underestimated owing to the narrow width of the NR[22].

In summary, we studied the channel length dependence of AB and AAS oscillations in Sb-doped Bi_2Se_3 TI NRs. Our observations demonstrate that the relative amplitudes of the AB and AAS oscillations can be adjusted by the channel length in comparison with the perimeter length of TI NR. The AAS oscillations are absent in short-channel devices in quasi-ballistic transport regime, while the AB oscillations are clearly observed even in a 70-μm-long device in diffusive regime. Thermal broadening and thermal dephasing effects are responsible for the exponential temperature dependence of the AB and AAS oscillations, respectively. Our observations suggest that the channel length in TI NR can be a useful tool for tailoring quantum interference effects combined with topological surface states.

Methods

Device fabrication. Sb-doped Bi_2Se_3 NRs were synthesized via chemical vapor deposition method in a horizontal tube furnace. Detailed information is available elsewhere[37]. Energy-dispersive X-ray spectroscopy of the NRs revealed the atomic percentages of Bi, Sb, and Se of approximately 36.0%, 5.5%, and 58.5%, respectively (see Supplementary Fig. 1). After the growth was completed, individual $(Bi_{1-x}Sb_x)_2Se_3$ NRs were mechanically transferred onto a highly *n*-doped Si substrate covered with a 300-nm-thick SiO_2 layer. The Si substrate was used as a back gate electrode. Source and drain electrodes were defined using standard electron-beam lithography followed by the electron-beam evaporation of Ti (10 nm)/Au (200 nm). Prior to the metal deposition, the electron-beam resist residue and the native oxide layer on the surface of NR were removed using oxygen plasma treatment and by dipping into a 6:1 buffered oxide etch for 7 s.

Measurements. All electrical transport measurements were performed using a conventional lock-in technique in a four-probe configuration. We used a closed-cycle ^{4}He cryostat (Seongwoo Instruments Inc.) and ^{3}He refrigerator system (Cryogenic, Ltd.), which had base temperatures of 2.4 and 0.3 K, respectively.

Weak antilocalization correction along the perimeter of TI NR. The WAL correction using the boundary conditions of the cylindrical geometry is as follows:[11]

$$\delta G = \frac{L_{\mathrm{p}}}{L_{\mathrm{ch}}} \frac{e^2}{\pi h} \left[\log \frac{L_{\mathrm{ch}}}{\xi} + \sum_{n=1}^{\infty} \cos \frac{4\pi n \Phi}{\Phi_0} \log \left(1 - e^{-\pi n L_{\mathrm{p}} / L_{\mathrm{ch}}} \right) \right],$$

where L_p is the perimeter length of the NR, L_{ch} the channel length, and ξ the correlation length of the disorder potential. The line of best fit in Fig. 1f was obtained using ξ = 850 nm as a fitting parameter and L_p = 1.2 μm (for **D2**) considering a 5-nm-thick oxide layer[17, 21] on the surface (see Supplementary Fig. 2).

Figure Captions

Figure 1 | Channel length dependence of *h*/*e*- and *h*/2*e*-periodic oscillations. (**a**) SEM image of Sb-doped Bi_2Se_3 NR device (D2) with various L_{ch} in the same NR. Channel lengths between the electrodes were L_{ch} = 1, 2, 3, and 4 μm for electrode pairs 1-2, 3-4, 5-6, and 6-7, respectively. Those pairs were used to measure voltage differences while a bias current was flowing through the entire NR. (**b**) Tilted-view SEM image of NR segment between 3-4 electrodes. (**c**) Conductance variation, δG, *vs.* axial magnetic field, B_{axial} curves obtained from NR segment (1-2) with L_{ch} = 1 μm for two different gate voltages, V_g at T = 2.4 K. Magnetic flux is denoted by Φ/Φ_0. (**d**) Color plot of δG as a function of B_{axial} and V_g for different L_{ch}. (**e**) Ensemble-averaged FFT amplitudes of $\delta G(B_{axial})$ curves for different L_{ch}. (**f**) FFT peak heights corresponding to *h*/*e*- and *h*/2*e*-periodic oscillations as a function of L_{ch}. The solid line is from the theoretical fit to the WAL correction (see Methods), whereas the dashed one from $L_{ch}^{-3/2}$ dependence (see text).

Figure 2 | *h*/*e*- and *h*/2*e*-periodic oscillations in long-channel devices. (**a**) SEM image of $(Bi_{0.89}Sb_{0.11})_2Se_3$ NR device (D6) with channel lengths of L_{ch} = 5 and 70 μm. Bias current was applied between a pair of electrodes numbered 1 and 5, whereas voltage difference was measured between electrodes 3 and 4 (2 and 3) electrodes for L_{ch} = 70 (5) μm. $\delta G(B_{axial})$ curves at different V_g and color plot of $\delta G(B_{axial}, V_g)$ at 2.6 K for (**b**) L_{ch} = 5 μm and (**c**) L_{ch} = 70 μm. $\delta G(B_{axial})$ curves were offset vertically for clarity. (**d**) Normalized ratio plot of ensemble-averaged FFT spectra with various L_{ch}. *h*/*e* (*h*/2*e*) oscillations are indicated by red (blue) arrows.

Figure 3 | Temperature dependence of FFT for *h*/*e* and *h*/2*e* period oscillations. Color plot of $\delta G(B_{axial}, V_g)$ at different temperatures for (**a**) L_{ch} = 2 μm, (**b**) 5 μm, and (**c**) 70 μm. Ensemble-averaged FFT amplitudes of $\delta G(B_{axial})$ curves at different temperatures for (**d**) L_{ch} = 2 μm, (**e**) 5 μm, and (**f**) 70 μm. FFT curves were averaged for all measured V_g. Temperature dependence of FFT peak heights of *h*/*e* and *h*/2*e* oscillations for (**g**) L_{ch} = 2 μm, (**h**) 5 μm, and (**i**) 70 μm. Solid lines are best fit results with damping parameters b_i ($i = h/e$, $h/2e$) (see text).

Data availability

The data that support the findings of this study are available from the corresponding author upon reasonable request.

References

1. Aharonov Y, Bohm D. Significance of Electromagnetic Potentials in the Quantum Theory. *Physical Review* **115**, 485-491 (1959).
2. Webb RA, Washburn S, Umbach CP, Laibowitz RB. Observation of *h*/*e* Aharonov-Bohm Oscillations in Normal-Metal Rings. *Physical Review Letters* **54**, 2696-2699 (1985).
3. Datta S*, et al.* Novel Interference Effects between Parallel Quantum Wells. *Physical Review Letters* **55**, 2344-2347 (1985).
4. Russo S*, et al.* Observation of Aharonov-Bohm conductance oscillations in a graphene ring. *Physical Review B* **77**, 085413 (2008).
5. Umbach CP, Van Haesendonck C, Laibowitz RB, Washburn S, Webb RA. Direct observation of ensemble averaging of the Aharonov-Bohm effect in normal-metal loops. *Physical Review Letters* **56**, 386-389 (1986).
6. Sharvin DY, Sharvin YV. Magnetic-flux quantization in a cylindrical film of a normal metal. *JETP Letters* **34**, 272-275 (1981).
7. Aronov AG, Sharvin YV. Magnetic flux effects in disordered conductors. *Reviews of Modern Physics* **59**, 755-779 (1987).
8. Bachtold A*, et al.* Aharonov-Bohm oscillations in carbon nanotubes. *Nature* **397**, 673-675 (1999).
9. Jung M*, et al.* Quantum Interference in Radial Heterostructure Nanowires. *Nano Letters* **8**, 3189-3193 (2008).
10. Al'tshuler B, Aronov A, Spivak B. The Aharonov-Bohm effect in disordered conductors. *JETP Letters* **33**, 94 (1981).
11. Bardarson JH, Brouwer PW, Moore JE. Aharonov-Bohm oscillations in disordered topological insulator nanowires. *Physical Review Letters* **105**, 156803 (2010).
12. Zhang Y, Vishwanath A. Anomalous Aharonov-Bohm conductance oscillations from topological insulator surface states. *Physical Review Letters* **105**, 206601 (2010).
13. Hasan MZ, Kane CL. Colloquium: Topological insulators. *Reviews of Modern Physics* **82**, 3045-3067 (2010).
14. Hong SS, Zhang Y, Cha JJ, Qi XL, Cui Y. One-dimensional helical transport in topological insulator nanowire interferometers. *Nano Letters* **14**, 2815-2821 (2014).
15. Cook A, Franz M. Majorana fermions in a topological-insulator nanowire proximity-coupled to an s-wave superconductor. *Physical Review B* **84**, 201105 (2011).
16. Peng H*, et al.* Aharonov-Bohm interference in topological insulator nanoribbons. *Nature Materials* **9**, 225-229 (2010).
17. Dufouleur J*, et al.* Quasiballistic Transport of Dirac Fermions in a Bi_2Se_3 Nanowire. *Physical Review Letters* **110**, 186806 (2013).
18. Cho S*, et al.* Aharonov-Bohm oscillations in a quasi-ballistic three-dimensional topological insulator nanowire. *Nature Communications* **6**, 8634 (2015).
19. Xiu F*, et al.* Manipulating surface states in topological insulator nanoribbons. *Nature Nanotechnology* **6**, 216-221 (2011).
20. Jauregui LA, Pettes MT, Rokhinson LP, Shi L, Chen YP. Magnetic field-induced helical mode and topological transitions in a topological insulator nanoribbon. *Nature Nanotechnology* **11**, 345-351 (2016).
21. Kim H-S, Shin HS, Lee JS, Ahn CW, Song JY, Doh Y-J. Quantum electrical transport properties of topological insulator Bi_2Te_3 nanowires. *Current Applied Physics* **16**, 51-56 (2016).

22. Kim J, *et al.* Quantum Electronic Transport of Topological Surface States in β-Ag_2Se Nanowire. *ACS Nano* **10**, 3936-3943 (2016).
23. Wang L-X, Li C-Z, Yu D-P, Liao Z-M. Aharonov–Bohm oscillations in Dirac semimetal Cd_3As_2 nanowires. *Nature Communications* **7**, 10769 (2016).
24. Sacksteder IV VE, Wu Q. Quantum interference effects in topological nanowires in a longitudinal magnetic field. *Physical Review B* **94**, 205424 (2016).
25. Washburn S, Webb RA. Aharonov-Bohm effect in normal metal quantum coherence and transport. *Advances in Physics* **35**, 375-422 (1986).
26. Stone AD, Imry Y. Periodicity of the Aharonov-Bohm effect in normal-metal rings. *Physical Review Letters* **56**, 189 (1986).
27. Bardarson JH, Moore JE. Quantum interference and Aharonov-Bohm oscillations in topological insulators. *Reports on Progress in Physics* **76**, 056501 (2013).
28. Kayyalha M, *et al.* Anomalous Low-Temperature Enhancement of Supercurrent in Topological-Insulator Nanoribbon Josephson Junctions: Evidence for Low-Energy Andreev Bound States. *Physical Review Letters* **122**, 047003 (2019).
29. Kim N-H, Kim H-S, Hou Y, Yu D, Doh Y-J. Superconducting quantum interference devices made of Sb-doped Bi_2Se_3 topological insulator nanoribbons. *Current Applied Physics* **20**, 680 (2020).
30. Mellnik AR, *et al.* Spin-transfer torque generated by a topological insulator. *Nature* **511**, 449 (2014).
31. Hwang T-H, Kim H-S, Kim H, Kim JS, Doh Y-J. Electrical detection of spin-polarized current in topological insulator $Bi_{1.5}Sb_{0.5}Te_{1.7}Se_{1.3}$. *Current Applied Physics* **19**, 917 (2019).
32. Kim M, *et al.* Nanomechanical characterization of quantum interference in a topological insulator nanowire. *Nature Communications* **10**, 4522 (2019).
33. Lee PA, Stone AD. Universal Conductance Fluctuations in Metals. *Physical Review Letters* **55**, 1622 (1985).
34. Lin K-T, Lin Y, Chi CC, Chen JC, Ueda T, Komiyama S. Temperature- and current-dependent dephasing in an Aharonov-Bohm ring. *Physical Review B* **81**, 035312 (2010).
35. Hansen AE, Kristensen A, Pedersen S, Sørensen CB, Lindelof PE. Mesoscopic decoherence in Aharonov-Bohm rings. *Physical Review B* **64**, 045327 (2001).
36. Kobayashi K, Aikawa H, Katsumoto S, Iye Y. Probe-Configuration-Dependent Decoherence in an Aharonov–Bohm Ring. *Journal of the Physical Society of Japan* **71**, 2094 (2002).
37. Hou Y, *et al.* Millimetre-long transport of photogenerated carriers in topological insulators. *Nature Communications* **10**, 5723 (2019).

Acknowledgements

This study was supported by the NRF of Korea through the Basic Science Research Program (2018R1A3B1052827) and the SRC Center for Quantum Coherence in Condensed Matter (2016R1A5A1008184). The work at UC Davis was supported by the U.S. National Science Foundation (Grant DMR-1838532). We are grateful to A. Morpurgo, K. Kang, J. H. Bardarson, and L. Rokhinson for their useful discussions.

Author contributions

H.-S.K. and T.-H.H. contributed equally to this study. Y.-J.D. designed the experiments and supervised the project. Y.H. and D.Y. grew the nanoribbons and conducted structural analysis. H.-S.K. and T.-H.H. fabricated the devices and performed the experiments. N.-H.K. assisted in sample fabrication and low-temperature measurements. H.-S.S. performed theoretical modeling, whereas H.-S.K., H.-S.S., and Y.-J.D. analyzed the data. H.-S.K. and Y.-J.D. prepared the manuscript. All the authors contributed to the discussion and paper preparation.

Competing interests

The authors declare no competing interests.

Additional information

Correspondence and requests for materials should be addressed to Y.-J.D.

Figure 1

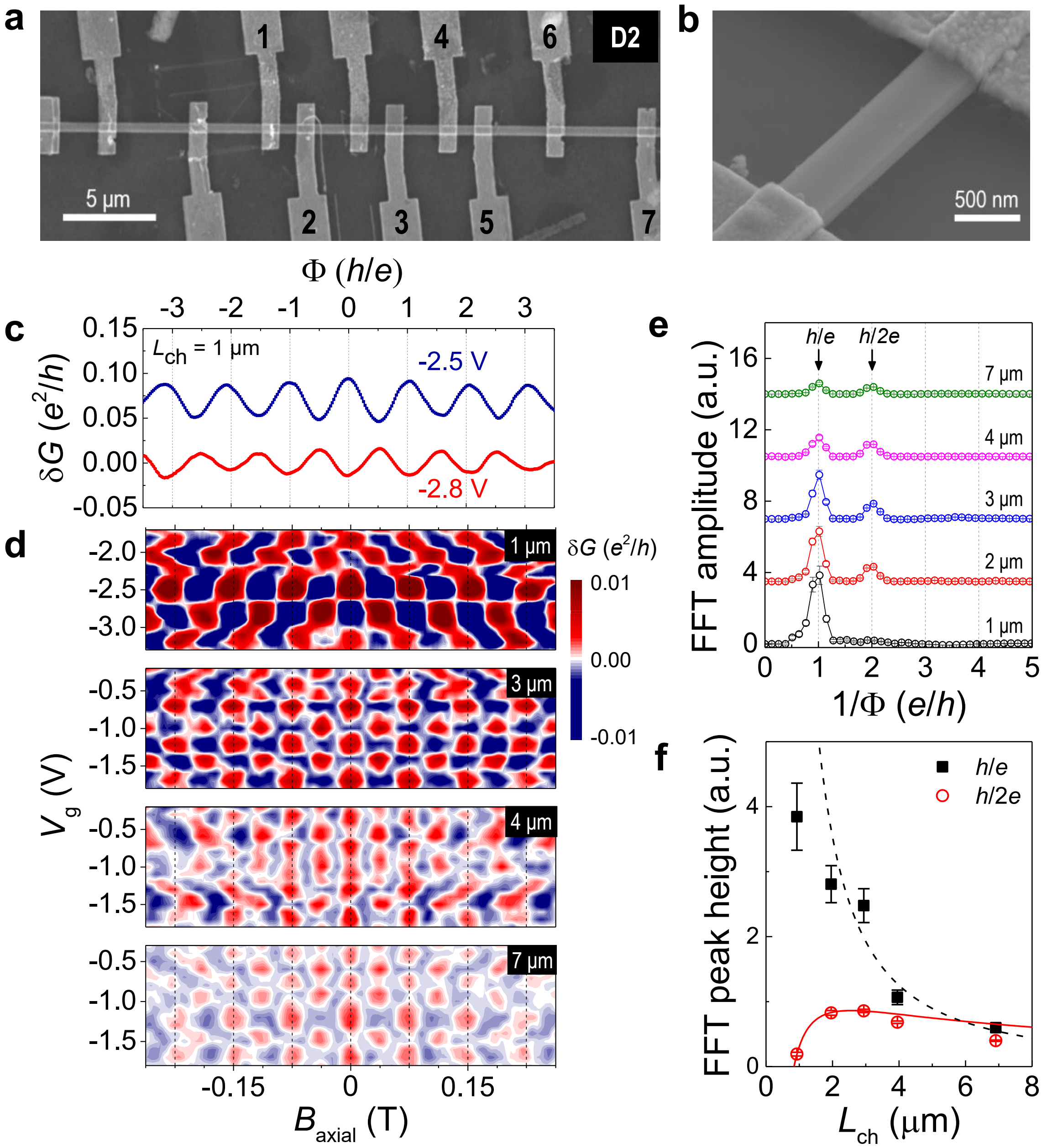
a
b
c
d
e
f
D2
1
2
3
4
5
6
7
5 μm
500 nm
Φ (h/e)
L_ch = 1 μm
-2.5 V
-2.8 V
δG (e²/h)
1 μm
3 μm
4 μm
7 μm
V_g (V)
B_axial (T)
h/e
h/2e
FFT amplitude (a.u.)
1/Φ (e/h)
2 μm
FFT peak height (a.u.)
L_ch (μm)

Figure 2

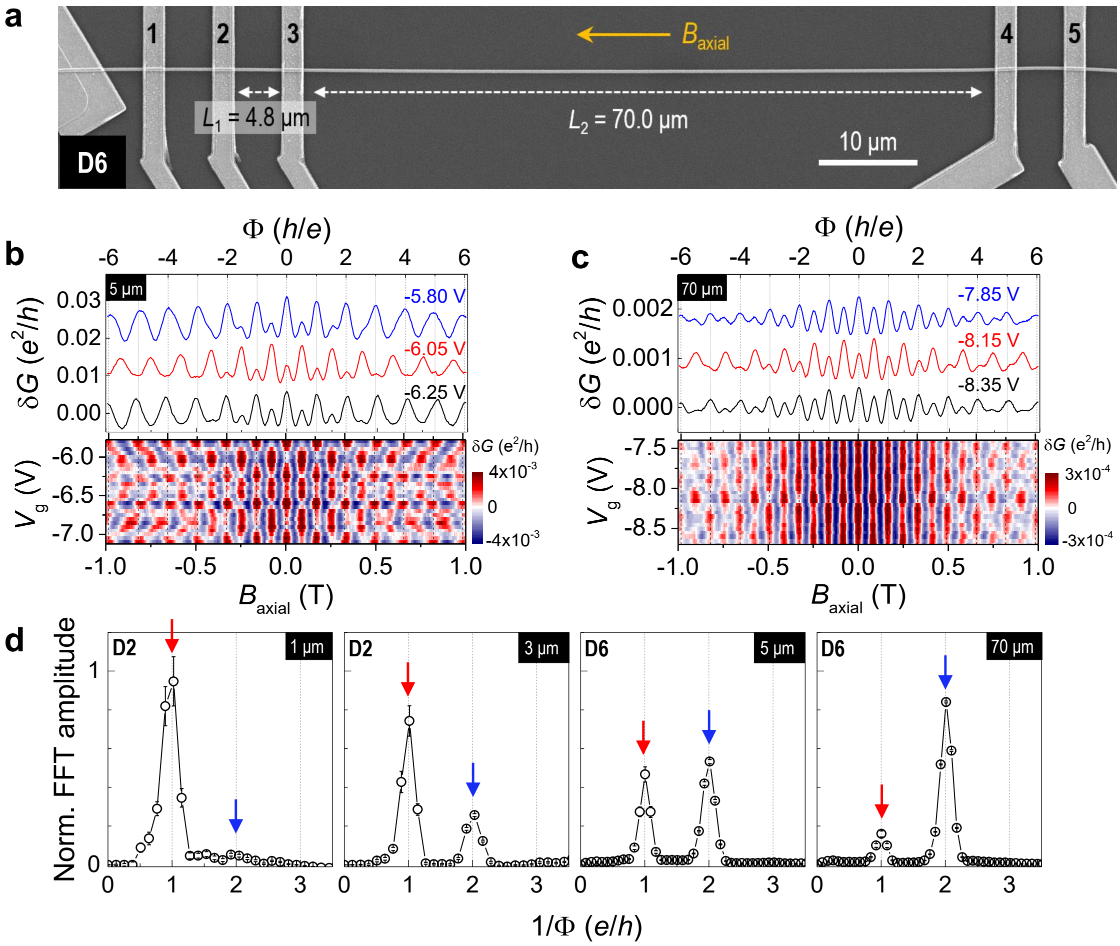
a
1
2
3
4
5
B_axial
L1 = 4.8 μm
L2 = 70.0 μm
10 μm
D6
b
Φ (h/e)
5 μm
-5.80 V
-6.05 V
-6.25 V
δG (e²/h)
Vg (V)
4x10⁻³
0
-4x10⁻³
B_axial (T)
c
Φ (h/e)
70 μm
-7.85 V
-8.15 V
-8.35 V
δG (e²/h)
Vg (V)
3x10⁻⁴
0
-3x10⁻⁴
B_axial (T)
d
Norm. FFT amplitude
D2
1 μm
D2
3 μm
D6
5 μm
D6
70 μm
1/Φ (e/h)

Figure 3

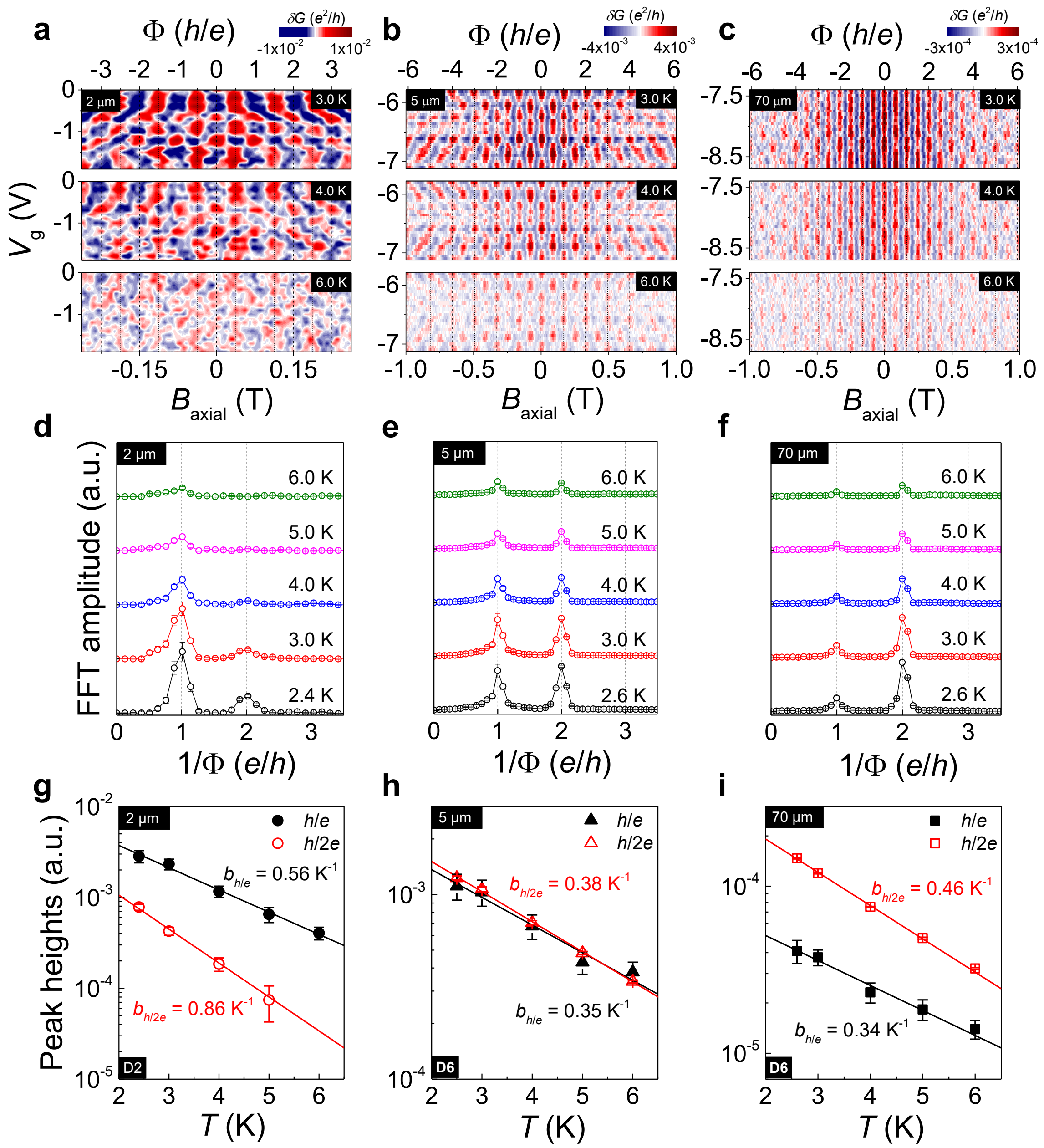

a
b
c
d
e
f
g
h
i
Φ (h/e)
δG (e²/h)
-1x10⁻²
1x10⁻²
-4x10⁻³
4x10⁻³
-3x10⁻⁴
3x10⁻⁴
2 μm
5 μm
70 μm
3.0 K
4.0 K
6.0 K
Vg (V)
Baxial (T)
FFT amplitude (a.u.)
2.4 K
2.6 K
5.0 K
1/Φ (e/h)
Peak heights (a.u.)
h/e
h/2e
bh/e = 0.56 K⁻¹
bh/2e = 0.86 K⁻¹
bh/2e = 0.38 K⁻¹
bh/e = 0.35 K⁻¹
bh/2e = 0.46 K⁻¹
bh/e = 0.34 K⁻¹
D2
D6
T (K)